

NANO EXPRESS

Open Access



Melting of Pb Nanocrystals Embedded in Al, Si, and Cu Matrices

Huan Wang* and Hongzhi Zhu

Abstract

Dispersions of nanoscale Pb particles embedded in Si, Al, and Cu matrices have been synthesized by ion implantation and subsequent annealing. The melting transitions of the embedded Pb nanocrystals with epitaxial particle/matrix interfaces were investigated by means of in situ high-temperature X-ray diffraction. Due to different levels of lattice mismatch, the Pb nanoprecipitates experience a different elastic strain in different matrices. Further analysis on the lattice constants of the embedded Pb nanocrystals gives unambiguous evidence of the strain-related pressure effect, which is particle size and matrix dependent, on tuning of the melting behavior of the embedded Pb nanoparticles.

Keywords: Ion implantation, Nanoparticles, Melting

Background

The melting behavior of low-dimensional solids, such as thin films, nanofibers, and nanoparticles, has drawn increasing attention in the past decades due to a fundamental understanding of their melting behavior at surfaces/interfaces and practical concerns of their technological application. Abundant experimental evidence shows that the melting point of nanoparticles and thin films can be considerably lowered compared to the equilibrium melting point of the corresponding bulk solids (T_0) [1–6]. The physical origin of this phenomenon lies on the fact that surface or interface atoms have a lower coordination, on average, and are thus more weakly bound and less constrained in their thermal motion than the atoms in the bulk. When the dimension of a solid is reduced, a larger fraction of surfaces/interfaces is provided, where melting nucleation may take place and the melting temperature will be lowered. However, when metal particles are coated by (or embedded in) a solid matrix with a high melting point, their thermal stability against melting can be enhanced, i.e., the melting point T_m can be even higher than T_0 . In 1986, Daeges et al. [7] demonstrated that Ag particles coated by Au could be heated up to 25 K above T_0 for 1 min without melting.

Following this pioneering work, superheating has been observed in a number of low- T_0 metal particles (with

sizes usually in the nanometer range) [8–12]. Further investigations indicated that two major effects are responsible for the observed superheating. The first one is the formation of low-energy *epitaxial* particle/matrix interfaces. Suppressed nucleation of the molten phase at epitaxial interfaces is considered a key factor controlling the superheating of these particles [4, 10, 13]. The second one is the pressure effect. A compressive pressure is exerted on embedded particles prior to melting due to the larger thermal expansion coefficient of metallic particles compared to that of the matrix. The pressure buildup was considered to be effective in raising the melting point of encapsulated/embedded nanoparticles. For example, a superheating as large as 270 K was observed in encapsulated metal particles (Pb, Sn) in fullerene-like shells [8]. This can be understood following the classical thermodynamic Clausius-Clapeyron consideration, which relates the change of pressure (dP) to the change of melting point (dT_m):

$$dT_m = \frac{dT_0 \Delta V}{L} \quad (1)$$

where L is the latent heat and ΔV is the relative volume change on melting [14]. For Pb, $\Delta V = (V_L - V_S)/V_S = 0.035$, V_S and V_L are the volumes of the solid and liquid phases, respectively. For an implanted system, the lattice mismatch between particles and matrix leads to additional pressure on embedded nanocrystals (NCs) via the epitaxial particle/matrix interface. However, in the

* Correspondence: wanghuan_2001@163.com
Chinese Academy of Engineering Physics, P. O. Box 919-71, Mianyang
621900, People's Republic of China

existing literature, the role of pressure appears to be small [10], or the strain-related pressure effect was not quantitatively analyzed [15].

To this end, we have synthesized Pb NCs embedded in crystalline Si, Al, and Cu matrices by using high-fluence ion implantation and subsequent annealing. Previous investigations show that the ion beam-synthesized Pb NCs have epitaxial particle/matrix interfaces and a well-defined octahedral shape bounded by {111} and {001} planes [11, 15, 16]. The average particle size can be tuned by different synthesis parameters such as implantation fluence and annealing time. In addition, different levels of lattice mismatch between bulk Pb and the crystalline matrices result in different strain in the embedded Pb NCs, ranging from compressive to tensile. This degree of freedom provides a handle to explore the strain-related pressure effect on the melting behavior of these embedded Pb NCs. In situ high-temperature X-ray diffraction (XRD) was used to monitor the melting of the embedded Pb NCs. This technique has several advantages: (i) by recording the diffraction signal as a function of temperature, the melting sequence of the material of interest can be *continuously* monitored; (ii) a quantitative correlation between the melting point and the particle size can also be obtained through the analysis of the diffraction profile; and (iii) it provides detailed information about the lattice parameters, i.e., the pressure exerted on the particles, as a function of temperature prior to melting. Such information is crucial to elucidate the role of pressure on the melting behavior of the embedded Pb NCs, which is not available from differential scanning calorimetry [17] or channeling analysis [15].

Methods

Epitaxial Al and Cu layers with a thickness of 150 nm have been grown on 7×7 reconstructed Si(111) and MgO(220) substrates, respectively, in a molecular beam epitaxy setup with a base pressure of 5×10^{-11} Torr. The deposition rate (~ 0.2 Å/s) was monitored in situ with a quartz crystal microbalance which was calibrated by using X-ray reflectivity. After deposition, the epitaxial layers were annealed in situ at 350 °C for 2 h in order to improve their crystalline quality.

Single-crystal Si(100) wafers and the epitaxial Al(111) and Cu(220) layers were implanted with 80 keV Pb⁺ ions at room temperature. The ion implantation current density was maintained below $2 \mu\text{Acm}^{-2}$ to reduce sample heating. After implantation, the samples with different implantation fluences ranging from 0.5×10^{16} to $4.0 \times 10^{16} \text{ cm}^{-2}$ were annealed in a N₂ atmosphere (Si) at 873 K for 45 min or in vacuum (Al and Cu) at 723 K for 60 min to promote Pb precipitation

and to recover the implantation-induced lattice damage to matrix materials.

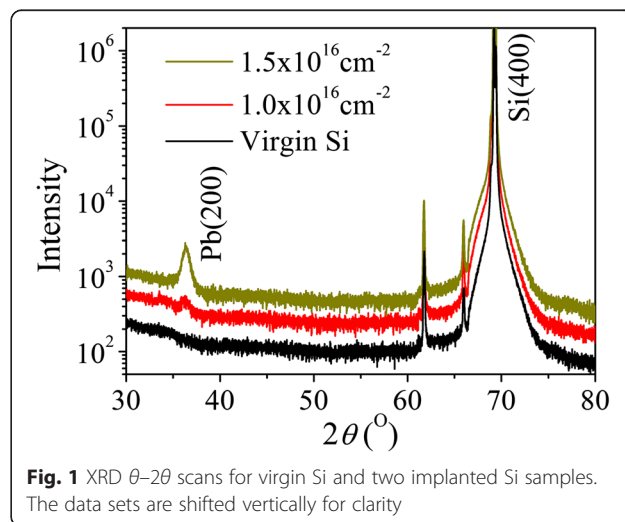
Conventional room temperature XRD was performed on a Bruker D8 diffractometer, using Cu K α radiation with an X-ray wavelength of 0.1542 nm. We used θ - 2θ scans to measure the average size of the crystalline Pb precipitates and their lattice constants. XRD azimuthal Φ scans combined with high-resolution transmission electron microscopy (HRTEM) measurements performed on a JEOL 4000 operated at 400 kV were used to determine the lattice structure, crystallographic orientation, and shape of the embedded Pb particles.

The melting behavior of the Pb NCs was monitored by a similar diffractometer equipped with a high-temperature attachment which allows measurements up to 1273 K. Symmetric θ - 2θ scans with a scan speed of $0.6^\circ/\text{min}$ were employed to monitor the diffraction signals from Pb NCs. The sample was mounted on a molybdenum base furnace and kept in a He gas flow in order to reduce the temperature gradient from the heater to the sample surface. The temperature was calibrated with an accuracy of ± 2 K by recording the Au-Si and Al-Si eutectics at 636 and 850 K, respectively. The sample was heated to each temperature at a heating rate of 5 K/min and held for 2 min before collecting the XRD profiles. During the measurements, the temperature stability was approximately 0.2 K.

Results and Discussion

Structural Characterization

Immediately after ion implantation and subsequent annealing, the structure of the Pb NCs was assessed by conventional XRD. Figure 1 shows θ - 2θ scans in a 2θ range of 30° – 80° for the Pb NCs in Si synthesized with different implantation fluences. The two small sharp peaks located at 61.6° and 65.8° are due to contributions

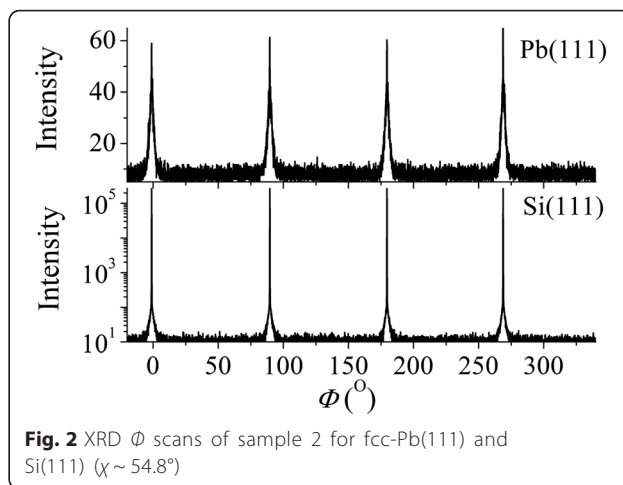


of the residual Cu K_β and Ni K_α radiation to the Si(400) diffraction peak, respectively. The only detectable Pb peak is the Pb(200) reflection at $2\theta \approx 36.3^\circ$, confirming that the Pb particles are highly oriented with respect to the host Si matrix [16]. The Pb diffraction peaks sharpen with increasing fluence, indicating the increasing size of the Pb NCs. By using the Scherrer formula, the average grain radius $\langle R \rangle$ is estimated (Table 1). The error on the experimental data is mainly due to the systematic variation of the background signal, leading to a varying width for the Pb diffraction peak after background subtraction.

Azimuthal Φ scans of the diffraction planes not parallel with the sample surface (i.e., tilted by an angle χ from the sample surface) help to determine the Pb NCs lattice structure as well as to reveal their in-plane crystallographic orientation with respect to the Si matrix. Figure 2 shows Φ scans of sample 2 for the Pb(111) diffraction with $2\theta \approx 31.3^\circ$ and the Si(111) diffraction with $2\theta \approx 28.5^\circ$, respectively. The fourfold symmetry, with $\chi \approx 54.8^\circ$, is consistent with the fcc-Pb(111) Φ scan. The peak positions of Pb(111) are coincident with the ones of Si(111), indicating an epitaxial relationship between the Pb NCs and the Si matrix. Therefore, we conclude that the fcc-Pb NCs are crystallographically oriented with respect to the Si matrix according to Pb(200)[002]//Si(200)[002]. The orientation of the Pb NCs in Al and Cu is determined as Pb(111)[11 $\bar{2}$]/Al(111)[11 $\bar{2}$] and Pb(220)[002]//Cu(220)[002], respectively, consistent with previous investigations [11, 15] and indicating an epitaxial alignment between the Pb NCs and the crystal-line matrices.

The faceted epitaxial Pb/Si interfaces were evident in the HRTEM image of a Pb NC in Si (sample 1) shown in Fig. 3. In addition, the hexagonal shape of the Pb particle when projected along the Si[011] zone axis indicates that the particle shape is a truncated octahedron bounded by {111} and {001} planes. This morphology of the Pb NCs in the Pb/Si system is very similar to that of the Pb particles in the Pb/Al and Pb/Cu systems [11, 15].

In order to accurately determine the lattice constants of the Pb NCs, XRD patterns from Pb NCs with different average particle radii $\langle R \rangle$ were carefully studied by symmetric θ - 2θ scans. The Pb(200) diffraction profiles



of the implanted Si samples are plotted in Fig. 4 after subtracting the background signal. Taking the Si(400) peak as a reference, the lattice constant a_{epi}^\perp of the Pb NCs is calculated. Subsequently, their perpendicular strain $e^\perp = (a_{\text{epi}}^\perp - a_0)/a_0$ is deduced, using $a_0 = 0.495$ nm for bulk (fully relaxed) Pb [18]. To determine the parallel lattice constant a_{epi}^\parallel and the in-plane strain e^\parallel , XRD θ - 2θ scans from the (220) diffraction were performed (not shown). According to the formula for d -spacing of a cubic crystal

$$d_{(hkl)}^2 = \frac{1}{\frac{k^2}{(a^\perp)^2} + \frac{l^2}{(a^\parallel)^2} + \frac{h^2}{(a^\parallel)^2}} \quad (2)$$

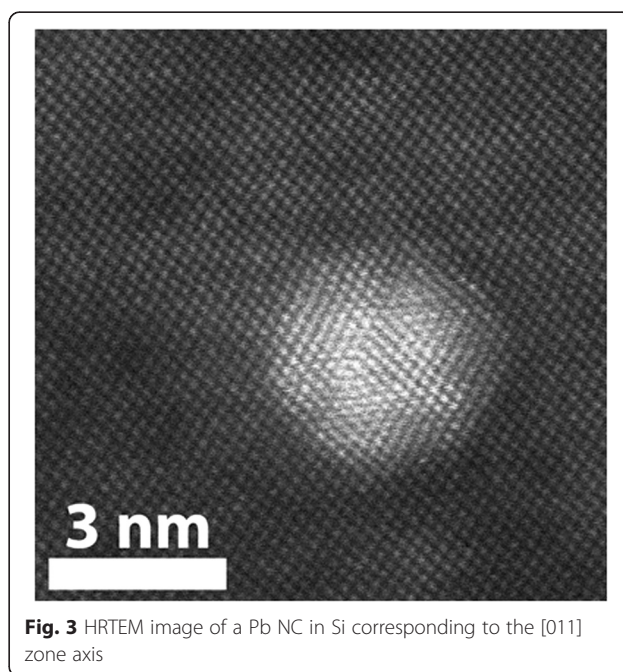
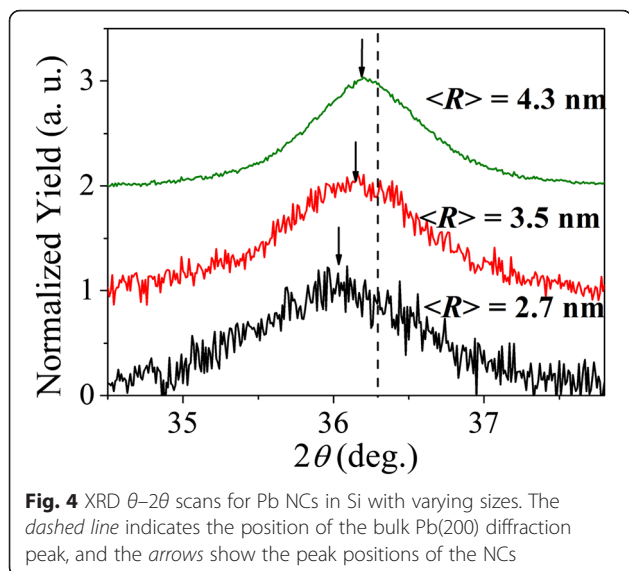


Table 1 Implantation fluence f and the average radius $\langle R \rangle$ of the embedded Pb NCs in different samples

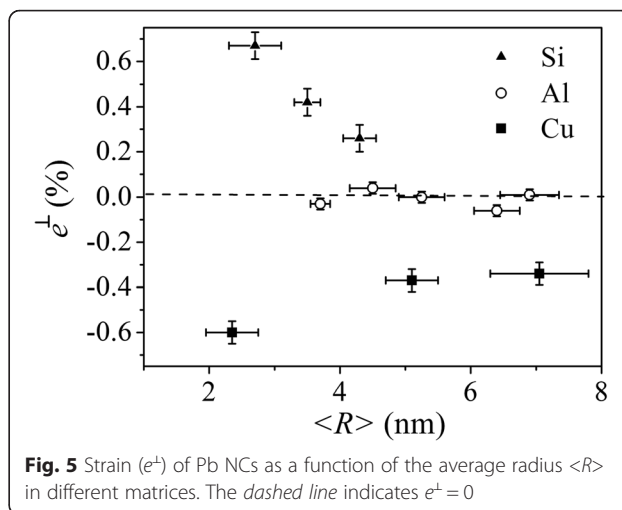
Sample no.	1	2	3	4	5
$f(10^{16} \text{ cm}^{-2})$	0.5	1.0	1.5	1.0	4.0
$\langle R \rangle$ (nm)	2.7 ± 0.2	3.5 ± 0.1	4.3 ± 0.1	6.7 ± 0.3	7.0 ± 0.3
Matrix	Si	Si	Si	Al	Cu



substituting the measured values of $d_{(220)}$, $a^\perp = a_{\text{epi}}^\perp$, and $k=2$, $l=2$, $h=0$ into the equation, we obtain the values for a_{epi}^\parallel . From this value, the parallel strain $e^\parallel = (a_{\text{epi}}^\parallel - a_0)/a_0$ can be calculated (Table 2). The results indicate that the lattice constant of the embedded Pb NCs in Si is isotropically enlarged. Such lattice constant tuning results from a uniform tensile strain ($e^\parallel \approx e^\perp$) generated at the epitaxial interfaces due to the negative lattice mismatch between the particle and the matrix, i.e., $a_{\text{Pb}} < a_{\text{Si}}$. For Pb NCs in Cu, the embedded Pb NCs exhibit lattice contraction since $a_{\text{Pb}} > a_{\text{Cu}}$, i.e., the embedded Pb NCs are under compressive strain (Fig. 5). With increasing particle size, a reduction of the tensile/compressive strain for the Pb NCs in Si/Cu is observed, which can be considered as a result of the lattice relaxation (due to the formation of misfit dislocations at the particle/matrix interfaces).

For the Pb NCs in Al, the lattice constants of bulk Pb and bulk Al follow $4a_{\text{Pb}} \approx 5a_{\text{Al}}$, corresponding to a relatively smaller lattice mismatch compared to the ones for Pb NCs in Si and Cu. The strain is expected to be easily released by interface misfit dislocations, and thus, no trace of strain is seen for the Pb NCs in the crystalline Al matrix as shown in Fig. 5.

From the measured lattice constants, one can estimate the strain-related pressure in the Pb NCs at room temperature to be



$$p = \frac{\kappa_{\text{Pb}} (a_0^3 - a_{\text{epi}}^3)}{a_0^3} \quad (3)$$

in which $K = 47.8$ GPa is the bulk modulus of lead [18]. Thus, different strain conditions indicate different pressure in the Pb NCs, which can be tuned by, e.g., particle size or matrix material. Consequently, Pb precipitates in these three matrices form an ideal system to investigate the strain-related pressure effect on the melting behavior of the embedded Pb NCs.

Melting Transition

Figure 6 presents in situ high-temperature XRD profiles of the Pb(200) diffraction peak of the embedded Pb NCs in Si at different fixed temperatures (sample 2). Although the intensity of the (200) peak decreases abruptly above 553 K, it is still clearly visible at 608 K, indicating that some Pb crystals exist in Si at a temperature which is 7 K higher than the T_m of bulk Pb. At 723 K, the diffraction peak of Pb has completely disappeared, implying that no Pb crystals survive at this temperature.

The dependence of the integrated Pb(200) diffraction intensity on temperature from the first, third, and fifth temperature sequences (covering the temperature regime of 350–650 K) is shown in Fig. 7 for sample 2. A hysteresis loop with a width ~ 50 K is clearly observed through several heating and cooling cycles and must hence be considered as an intrinsic phenomenon of the embedded Pb NCs in Si.

Table 2 Lattice constants and elastic strain of the Pb NCs in Si

Sample no.	Average radius (nm)	a_{epi}^\perp (nm)	a_{epi}^\parallel (nm)	e^\perp (%)	e^\parallel (%)
1	2.7 ± 0.2	0.4983 ± 0.0003	0.4982 ± 0.0006	0.67 ± 0.04	0.66 ± 0.13
2	3.5 ± 0.1	0.4971 ± 0.0003	0.4969 ± 0.0006	0.42 ± 0.04	0.37 ± 0.13
3	4.3 ± 0.1	0.4963 ± 0.0003	0.4961 ± 0.0006	0.26 ± 0.04	0.22 ± 0.13

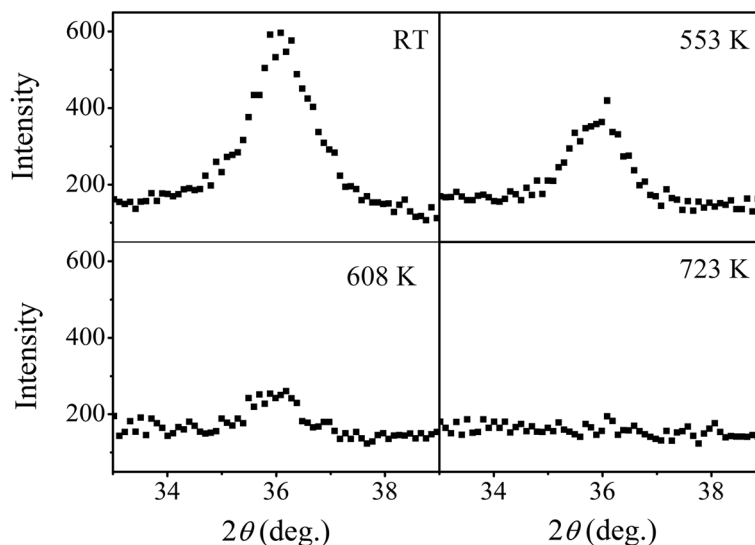


Fig. 6 High-temperature XRD profiles of the Pb(200) diffraction peak at different temperatures for sample 2. The average radius of Pb NCs in Si is about 3.5 nm

Figure 8 shows a logarithmic plot of the integrated intensity of the Pb(200) peak as a function of temperature in the third heating cycle (sample 2). For a crystal containing only one kind of atom, with increasing temperature, the enhanced thermal displacement of atoms attenuates the diffraction intensity, I , according to the Debye-Waller factor, $\exp[-2B(\sin\theta/\lambda)^2]$: $I = I_0 \exp[-2B(\sin\theta/\lambda)^2]$, where θ is the Bragg angle, λ is the wavelength of the X-rays, I_0 is the diffraction intensity of X-rays at 0 K, $B = 8\pi^2\langle u^2 \rangle$ is the Debye-Waller parameter, and $\langle u^2 \rangle^{1/2}$ is the root-mean-square (rms) atomic displacement [19]. It is worth emphasizing that for single-crystalline elemental materials, at temperatures much higher than the Debye temperature

Θ_D ($\Theta_D^{\text{Pb}} = 88$ K), $\langle u^2 \rangle^{1/2} = (3^2 T / M \kappa_B \Theta_D)^{1/2}$, i.e., $\langle u^2 \rangle$ is proportional to the absolute temperature T , where M is the mass of the atoms, κ_B is the Boltzmann constant, and \hbar is Planck's constant [19]. Thus, the rms displacement $\langle u^2 \rangle^{1/2} = -[\ln(I/I_0)]^{1/2} \lambda / 4\pi \sin\theta$ of Pb atoms can be obtained from the XRD data shown in Fig. 7. The Lindemann criterion [20] states that melting occurs when the atomic rms displacement exceeds 12 % of the nearest-neighbor distance for fcc bulk crystals [21]. This empirical criterion was proven valid for NCs [10] and thus was applied for the melting point determination of the embedded Pb NCs. For example, the melting of the embedded Pb NCs in sample 2 is determined to take place at 530 K, prior to which the rms displacement of the Pb atoms increases slowly to a value of ~12 % (see Fig. 8). At temperatures above 530 K, some of the Pb has melted with no contribution to the observed integrated intensity, and the calculated rms displacement values are unphysical. In addition, the average particle size determined from the width of Pb(200) after annealing is evident to be the same as the one after in situ high-temperature XRD measurements within the experimental error. That means the size evolution of the Pb nanoparticles during heating and cooling cycles of in situ high-temperature XRD measurement is too small to be neglected.

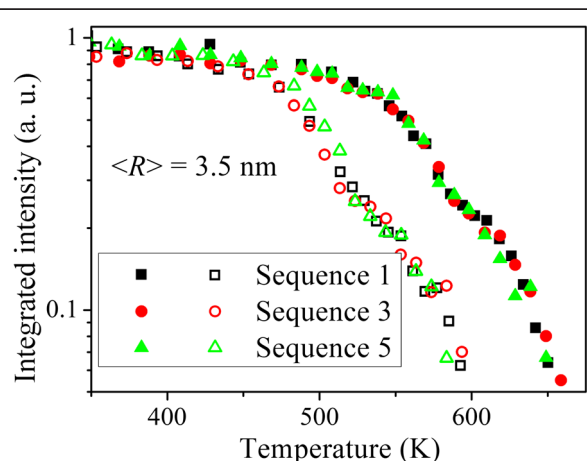


Fig. 7 Integrated intensity of Pb(200) as a function of temperature for sample 2. The solid and open symbols represent data during heating and cooling, respectively, in three temperature sequences

Melting of Pb NCs

The melting transitions for the embedded Pb NCs with different average sizes in Al are shown in Fig. 9, by plotting the integrated Pb(111) diffraction peak intensity as a function of temperature. A considerable superheating

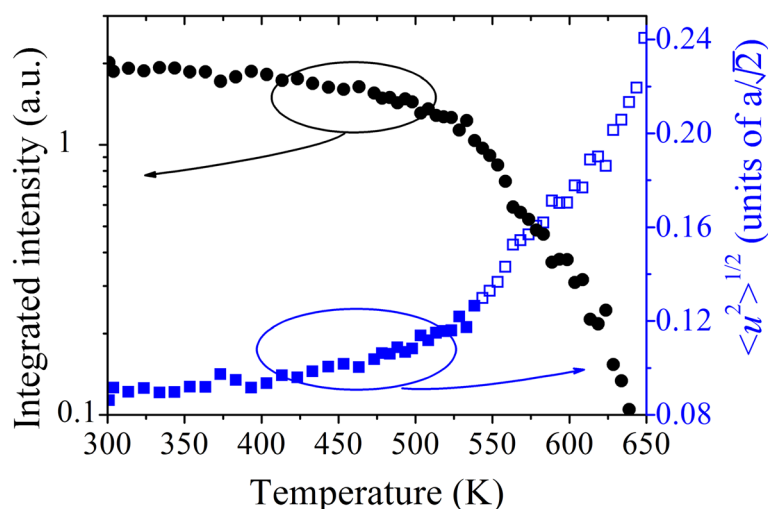


Fig. 8 The experimentally determined rms displacement of the lead atoms as a function of temperature (blue filled squares). Logarithmic plot of the integrated intensity for the Pb(200) diffraction peak (sample 2) during the heating up (black filled circles) is shown. Above 530 K, a fraction of the precipitates is melted, and the rms values shown (empty squares) are unphysical

during the warming up process is observed, an effect which is clearly particle size dependent.

In order to examine the pressure effect on the melting behavior of the embedded Pb particles in Al, the lattice constants of Pb NCs in sample 4 as a function of temperature is shown in Fig. 10. We find that the lattice parameters of the embedded particles with an average radius of 6.7 nm are within the error in agreement with the tabulated bulk values, which are calculated from the known bulk Pb thermal expansion coefficient [18]. From the lattice parameters of the Pb particles and the known bulk modulus of lead, the pressure in the Pb NCs was determined, as shown in Fig. 11. According to the Clausius-Clapeyron equation

(Eq. 1), these pressures would give rise to a maximum increase in the melting temperature of ~10 K. As this is significantly smaller than the observed superheating in the Pb NCs, the pressure effect alone can only be considered to play a minor role in their melting temperature elevation. This is not surprising because (i) the pressure exerted on the embedded Pb NCs induced by the elastic strain is found to be extremely low at room temperature and (ii) the pressure ΔP_T , imposed on the Pb NCs by matrix confinement upon heating due to the mismatch of thermal expansion coefficient between Pb and Al, is also small. The latter contribution can be calculated using the treatment of Spaepen and Turnbull [22]:

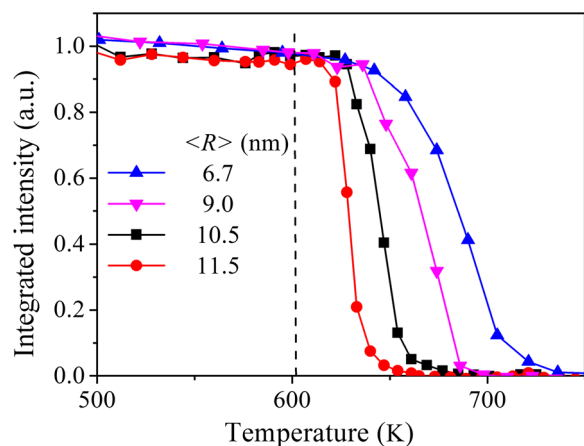


Fig. 9 Integrated intensity of the Pb(111) for Pb NCs in Al with different average radii $\langle R \rangle$. The dashed line marks the melting point of bulk Pb

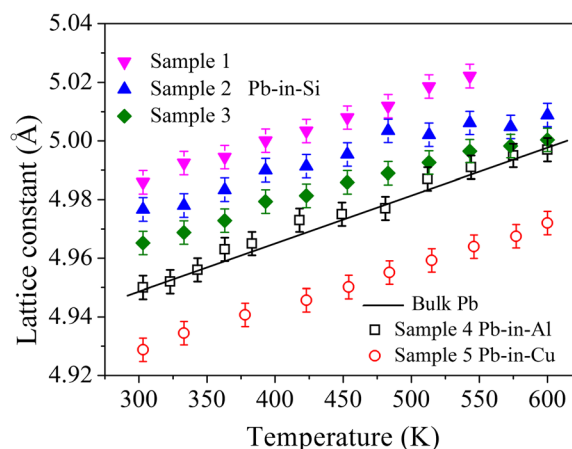


Fig. 10 Lattice constants of bulk Pb (—) and Pb NCs as a function of temperature

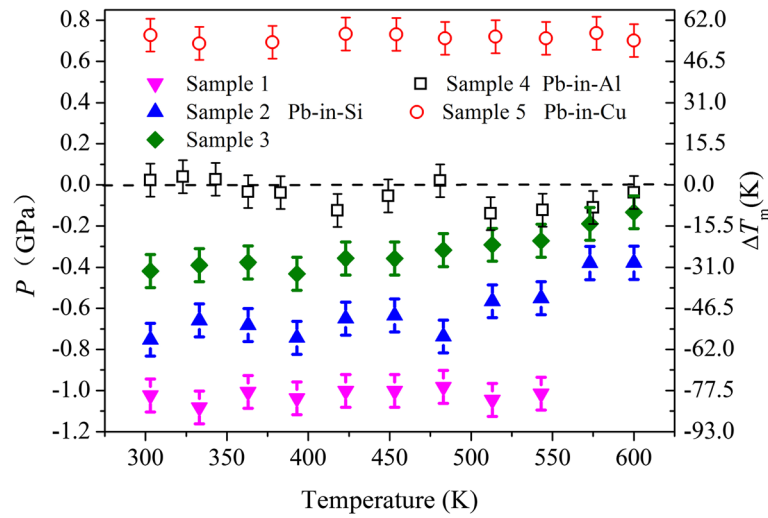


Fig. 11 The pressure and calculated change of melting point ΔT_m as a function of temperature. The dashed line marks $\Delta T_m = 0$

$$\Delta p_T = \frac{12(\alpha_{Pb} - \alpha_M)\Delta T \mu_M \kappa_{Pb}}{4\mu_M + 3\kappa_{Pb}} \quad (4)$$

where μ_M is the shear modulus of the matrix ($\mu_{Al} = 26$ GPa [18]), the α 's are the linear thermal expansion coefficients, and ΔT is the temperature increase on heating. Since the thermal coefficient of Pb is only slightly larger than that of Al ($\alpha_{Pb} = 2.89 \times 10^{-5} \text{ K}^{-1}$, $\alpha_{Al} = 2.31 \times 10^{-5} \text{ K}^{-1}$ [18]), a small compressive pressure of 0.04 GPa in Pb is built up when a Pb/Al sample is heated from room temperature to 600 K. This pressure corresponds to a ~ 4 K increase in the melting point, which is negligibly small. Thus, the superheating is mainly attributed to the low-energy epitaxial particle/matrix interfaces [10].

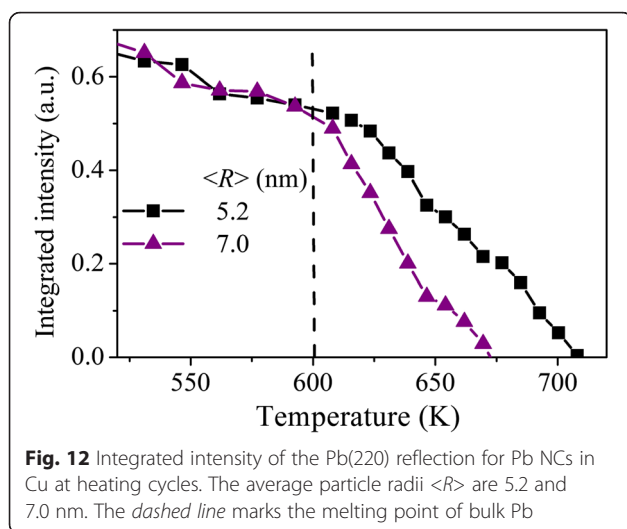
To fully explain the size-dependent melting point of embedded nanoparticles, Allen et al. [23] proposed a thermodynamic model, which includes both the pressure and particle/matrix interface effects. They derived a relationship between the melting temperature and the particle radius R as:

$$\frac{T_R}{T_0^{Pb}} = 1 - \frac{3}{QR} \left[\frac{\gamma_{SM}}{\rho_S} - \frac{\gamma_{LM}}{\rho_L} \right] + \frac{\Delta E}{Q} \quad (5)$$

where T_R and T_0^{Pb} are the melting temperatures for particles of radius R and for bulk material, respectively; γ_{SM} and γ_{LM} are the interfacial energies between the solid and the matrix and the liquid and the matrix; ρ_S and ρ_L are the densities of solid and liquid lead, respectively; Q is the latent heat of melting; and ΔE is the change of free energy upon melting due to matrix confinement [23]. For embedded spherical particles, $\Delta E = P\Delta V$, P is the pressure in the embedded particle prior to melting and ΔV is the relative volume change on melting (for lead, $\Delta V = 0.035$ [18]).

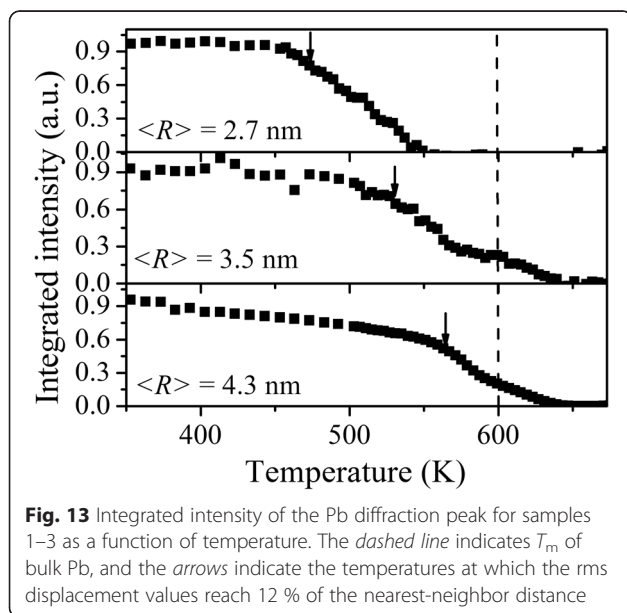
As demonstrated above in the discussion of the lattice parameters of Pb particles, the Clausius-Clapeyron equation shows that pressure, i.e., ΔE , cannot be the dominant term to explain superheating in Pb. Thus, the superheating of the embedded Pb particles is mainly attributed to the low-energy epitaxial Pb/Al interfaces, i.e., $\gamma_{SM} < \gamma_{LM}$, leading to a suppression of interface nucleation of the liquid phase as confirmed by molecular dynamics simulations [24]. Moreover, according to Eq. 3, the superheating decreases with increasing particle size, consistent with our observation. This can be understood based on the fact that with increasing particle size, due to the decreasing surface-to-volume ratio, the role of the low-energy Pb/Al interfaces in achieving superheating is suppressed.

Since the Pb inclusions exhibit a lattice contraction in Cu (Fig. 5), it may be envisaged that a compressive pressure plays an important role in achieving the superheating of Pb NCs in Cu [15], as shown in Fig. 12. To confirm this hypothesis, the lattice parameter of the Pb NCs in Cu as a function of temperature is shown in Fig. 10. For the Pb/Cu sample, $e^{\perp} < 0$ is observed. It means that a compressive pressure on the embedded Pb NCs is maintained prior to their melting, which leads to an enhancement of the melting temperature [20]. According to Eq. 2, the pressure Δp_T imposed on the embedded Pb NCs due to matrix confinement is ~ 0.16 GPa when the sample is heated up from room temperature to 600 K. That is smaller than the measured pressure for Pb NCs, 0.71 GPa, determined by their lattice constant at 600 K (Fig. 11). These findings imply that the compressive pressure exerted on the Pb NCs in Cu prior to their melting is due to both (i) the compressive strain and (ii) matrix confinement upon heating. In addition, the superheating of the Pb NCs in Cu cannot be only



due to the overpressure. For instance at 600 K, the measured pressure up to 0.71 GPa corresponds to an increase of 55 K in the melting temperature (Fig. 11). This is smaller than the observed superheating in Fig. 12. Thus, the superheating of the embedded Pb NCs in Cu is both attributed to the low-energy particle/matrix interface and the compressive pressure caused by the compressive strain and matrix confinement.

The melting transitions for the embedded Pb NCs with different average sizes in Si (samples 1–3) are shown in Fig. 13. The arrows indicate the temperatures at which melting of the Pb NCs takes place according to the Lindemann criterion. For the Pb/Si samples, the Pb NCs start to melt below the equilibrium temperature of bulk Pb and their melting temperature decreases with decreasing average size. From our experimental results,



it is clear that the melting behavior of the embedded Pb NCs cannot be fully explained by (i) the suppression of melting nucleation at the epitaxial particle/matrix interface and (ii) the pressure effect caused by matrix confinement, i.e., the difference in thermal expansion coefficients between the Pb particles and the Si matrix, which is particle size independent. That is because both effects result in *superheating* of the embedded Pb NCs. Naturally, we have to take the strain-related pressure effect into account based on the fact that the tensile strain is found in the Pb NCs at room temperature.

In order to evaluate the role of elastic strain-related pressure effect on the melting behavior of the embedded Pb NCs, their lattice parameters were extracted from the XRD data, as shown in Fig. 10. Then, the strain of the embedded Pb NCs as a function of temperature is obtained (Fig. 11). It can be seen that at high temperatures, tensile strain is still present for the Pb NCs in Si, i.e., $\epsilon^+ > 0$, indicating a negative pressure in the embedded Pb NCs, i.e., the Pb particles are subjected to tensile stresses. According to the Clausius-Clapeyron equation, this leads to a decrease of melting point. With increasing particle size, due to strain relaxation, a decrease of the tensile strain (i.e., the negative pressure) in the Pb particles is observed at temperatures prior to melting in Fig. 11. Thus, an enhancement of the melting point for the samples with larger particles is expected, consistent with our experimental results. This again shows unambiguously that the strain has to be taken into account in order to explain the melting behavior of Pb NCs embedded in Si. Hence, their melting can be interpreted in terms of two competing effects: (1) the melting temperature elevation by the low-energy epitaxial interfaces and the matrix confinement and (2) the suppression of the melting point due to the tensile strain-related pressure effect.

The above analysis gives further indication that the strain-related pressure effect can affect the melting behavior of the embedded Pb NCs. It is worth emphasizing that in contrast with the overpressure caused by the different thermal expansion coefficients between metallic nanoparticles and rigid matrices ($\alpha_{\text{particle}} < \alpha_{\text{Matrix}}$) [25], which leads to a melting point elevation, the strain-related pressure effect is evident to enhance or decrease the melting temperature depending on the lattice mismatch between the Pb NCs and the crystalline matrices with the epitaxial particle/matrix interfaces. In addition, compared to Pb particles in Al, the melting transition of the embedded Pb NCs in Si and Cu is much broader, which is attributed to the larger size distribution of the embedded Pb NCs in Si and Cu. Although the size distribution of the embedded Pb particles can broaden the melting transition, trends of the average size- and the elastic strain-

dependent melting are still clearly observed for these embedded Pb precipitates.

Conclusions

In conclusion, we have experimentally analyzed the melting behavior of Pb NCs in the crystalline Si, Al, and Cu matrices with epitaxial particle/matrix interfaces. Based on our detailed investigation of the lattice parameters of the embedded Pb NCs, we believe that the usual explanation advocated to explain superheating, i.e., interface epitaxy suppresses the melting nucleation, cannot fully account for the melting behavior of the embedded Pb NCs in Si and Cu. We demonstrated that the strain-related pressure effect plays an important role in controlling their melting behavior, which provides new possibilities to tune the instability temperature of low-dimensional materials against melting.

Competing Interests

The authors declare that they have no competing interests.

Authors' Contributions

HW designed the experiments and wrote the manuscript. HZ supervised the discussion part of the work. Both authors read and approved the final manuscript.

Acknowledgements

The work was supported by the National Natural Science Foundation of China under Grant No. 11505160 as well as the Director Foundation of Institute of Materials, Chinese Academy of Engineering Physics, under Grant No. SJZ201406. A part of the work was performed in KU Leuven, and the author HW thanks Prof. Dr. André Vantomme and Prof. Dr. Kristiaan Temst for their discussion.

Received: 28 October 2015 Accepted: 10 December 2015

Published online: 21 December 2015

References

- Couchman PR, Jesser WA (1977) Thermodynamic theory of size dependence of melting temperature in metals. *Nature* 269:481
- Takagi M (1954) Electron-diffusion study of liquid-solid transition of thin metal films. *J Phys Soc Jpn* 9:359
- Buffat P, Borel J-P (1976) Size effect on the melting temperature of gold particles. *Phys Rev A* 13:2287
- Cahn RW (1986) Materials science: melting and the surface. *Nature* 323:668
- Cahn RW (1989) New ideas for the melting pot. *Nature* 342:619
- Pluis B, Denier van der Gon AW, Van Der Veen JF, Riemersma AJ (1990) Surface-induced melting and freezing I. Medium-energy ion scattering investigation of the melting of Pb{hkl} crystal faces. *Surf Sci* 239:265
- Daeges J, Gleiter H, Perepezko JH (1986) Superheating of metal crystals. *Phys Lett A* 119:79
- Banhart F, Hernández E, Terrones M (2003) Extreme superheating and supercoiling of encapsulated metals in fullerene-like shells. *Phys Rev Lett* 90:185502
- Zhang DL, Cantor B (1991) Melting behavior of In and Pb particles embedded in an Al matrix. *Acta Metall Mater* 39:1959
- Gråbaek L, Bohr J, Johnson E, Johanson A, Sarholt-Kristensen L, Andersen HH (1990) Superheating and supercoiling of lead precipitates in aluminum. *Phys Rev Lett* 64:934
- Gråbaek L, Bohr J, Andersen HH, Johanson A, Johnson E, Sarholt-Kristensen L (1992) Melting, growth, and faceting of lead precipitates in aluminum. *Phys Rev B* 45:2628
- Andersen HH, Johnson E (1995) Structure, morphology and melting hysteresis of ion-implanted nanocrystals. *Nucl Instr Meth Phys Res B* 106:480
- Dahmen U, Xiao SQ, Paciornik S, Johnson E, Johansen A (1997) Magic-size equilibrium shapes of nanoscale Pb inclusions in Al. *Phys Rev Lett* 78:471
- Landau LD, Lifshitz EM (1980) Course on theoretical physics: statistical physics. Pergamon, Oxford
- Johansen A, Johnson E, Sarholt L, Dupont E, Anderson HH, Touboltsev VS (2002) Annealing reactions in lead implanted copper. *Nucl Instr Meth Phys Res B* 190:802
- Milants K, Verheyden J, Barancira T, Deweerdt W, Pattyn H, Bukshpan S, Williamson DL, Vermeiren F, Van Tendeloo G, Vlekken C, Libbrecht S, Van Haesendonck C (1997) Size distribution and magnetic behavior of lead inclusions in silicon single crystals. *J Appl Phys* 81:2148
- Sheng HW, Hu ZQ, Lu K (1997) Melting and freezing behaviors of Pb nanoparticles embedded in an Al matrix. *Nanostruct Mater* 9:661
- Brandes EA (1983) *Smithells metals reference book*. Butterworths, London
- Guinier A (1963) *X-ray diffraction, in crystals, imperfect crystals and amorphous bodies*. Freeman, San Francisco
- Lindemann FA (1910) The calculation of molecular vibration frequencies. *Zeitschrift Physikalisches* 14:609
- Cho SA (1982) Role of lattice structure on the Lindemann fusion theory of metals. *J Phys F Met Phys* 12:1069
- Spaepen F, Turnbull D (1979) Negative pressures and melting point depression in oxide-coated liquid metal droplets. *Scripta Metall* 13:149
- Allen GL, Gile WW, Jesser WA (1980) The melting temperature of microcrystals embedded in a matrix. *Acta Mater* 28:1695
- Lai SL, Carlsson JRA, Allen LH (1998) Melting point depression of Al clusters generated during the early stages of film growth: nanocalorimetry measurements. *Appl Phys Lett* 72:1098
- Mei MS, Wang SC, Cong HT, Jin ZH, Lu K (2005) Pressure-induced superheating of Al nanoparticles encapsulated in Al₂O₃ shells without epitaxial interface. *Acta Mater* 53:1059

Submit your manuscript to a SpringerOpen[®] journal and benefit from:

- Convenient online submission
- Rigorous peer review
- Immediate publication on acceptance
- Open access: articles freely available online
- High visibility within the field
- Retaining the copyright to your article

Submit your next manuscript at ► springeropen.com